Numerical Investigation on Feasibility of a Flight Experiment of the Traveling Liquidus-Zone Method

Satoshi Adachi [1], Naokiyo Koshikawa [1], Satoshi Matsumoto[1], Sadayoshi Yuge[1,*], Shin-ichi Yoda [2], and Kyoichi Kinoshita [2]

[1] Space Utilization Research Center, Office of Space Utilization Systems, National Space Development Agency of Japan, 2-1-1, Sengen, Tsukuba-shi, Ibaraki, 305-8505 Japan

[2] Space Utilization Research Program, National Space Development Agency of Japan, 2-1-1, Sengen, Tsukuba-shi, Ibaraki, 305-8505 Japan

Abstract

We have four major targets this year, that is, (i) to investigate validity of one-dimensional approximation in the case of a 10 mm-diameter sample, (ii) to design a dummy cartridge, (iii) to investigate influence of convection on the ground in the case of a 2 mm-diameter sample, and (iv) to investigate difference in the case of updated thermophysical properties. Before investigating the validity of one-dimensional approximation, we first investigated an optimal heat sink diameter. By using the optimal heat sink diameter, we found that one-dimensional approximation was valid under a certain boundary condition near a growth interface. We also applied the optimal heat sink diameter to design of a prototype dummy cartridge. We investigated the convection influence on concentration distribution by modeling a zone of 2 mm in diameter and of 20 mm in length under the 1 g condition. From the calculation results, it was found that the influence was negligibly small. The thermophysical properties were updated. The calculation results showed that temperature distribution and interface shapes were quite different from the results in the case of the older properties.

Introduction

The traveling liquidus-zone (TLZ) method [1] is one of the most advancing growth techniques to obtain a homogeneous crystal of a ternary compound semiconductor. By applying the TLZ method to crystal growth of an InGaAs compound semiconductor on the earth, single crystals of 2 mm in diameter and uniform composition of around 0.3 of indium have been grown to a distance more than 20 mm. The most valuable feature of the TLZ method is that the solution concentration is saturated and sustained at the concentration determined by the liquidus in the whole zone region. Based on this concept, we have already succeeded in establishing a one-dimensional theoretical model [2]. The model predicts that a growth rate can be controlled only by the temperature gradient at the freezing interface.

* The present affiliation: Showa Cabot K.K., Chiba Plant, 3-Yahatakaigandori, Ichihara-City, Chiba 290-0067, Japan

This means that if the linear temperature distribution inside the zone could be achieved, the constant growth rate could be maintained through the whole growth duration. This is a great advantage from a viewpoint of homogeneous growth as compared with the other growth techniques.

As mentioned above, the TLZ method is potentially one of the most suitable techniques to obtain homogeneous multicomponent single crystals. To establish the TLZ method, the one-dimensional model must be verified first. We think the microgravity condition is the most suitable environments to verify the model because convection suppression improves the one-dimensionality as compared with the ground environments. Therefore, we proposed an experimental plan to the International Announcement of Opportunity (IAO). At present, our plan is selected as a candidate for a flight experiment in the International Space Station (ISS).

In order to perform a microgravity experiment, an ampoule and a cartridge must be designed. Although a sample of 20 mm in diameter is planned before the IAO, the diameter is changed to 10 mm in the proposal from the viewpoint of one-dimensionality. But more investigation is required whether the 10 mm sample sufficiently satisfies the one-dimensionality.

To investigate the one-dimensionality, numerical analysis has been carried out. The calculation code can treat the TLZ growth and can solve the governing equations of the energy transport, the mass transport, the vorticity transport, and the stream function. The numerical analysis is used for not only investigating one-dimensionality but also optimizing a heat sink diameter in the case of the sample of 10 mm in diameter. By using the calculation results, we design a prototype dummy cartridge. The dummy cartridge will be used in the ground-based experiments in order to obtain the temperature profiles inside the cartridge under various furnace configurations. The experimentally obtained data will be compared with the numerically obtained data in future in order to verify the reliability of the numerical analysis.

After we proposed our plan to the IAO, understanding of the TLZ method has been deepened. We think there is possibility that the verification of one-dimensional model can be achieved by using samples of 2 mm or less in diameter even though on the ground. Thus the influences of the convection on concentration and temperature distributions are numerically investigated in the case of the 2 mm sample.

Thermophysical properties of InGaAs have been measured in parallel to the activities mentioned above. Therefore we compare the numerical results in the case of the updated properties with those in the case of the older properties in order to understand the difference.

In this paper, the mathematical model is described in the next section, and then the calculation results in the case of the 10 mm-diameter sample, the dummy cartridge design, the convection influence in the case of 2mm sample, and the difference between the older properties case and the newest properties case are described. After that, discussion and conclusions are described.

Mathematical Model

The governing equations are the energy transport equation, the mass transport equation, the vorticity transport equation, the stream function equation, the energy balance equation and the mass balance equation. We use the boundary fitted coordinate (BFC) method [3-9], which is a kind of

finite difference method, in order to solve these equations in this paper. The BFC method solves the governing equations that are transformed from the physical space to the computational space. Therefore, curved boundaries in the physical space are transformed to linear ones. In addition, the coordinates are transformed to the rectangular coordinates in the computational space. The governing equations, which are transformed to the computational space, are described as Eqs. (1) – (7). The detailed transformation procedure is described in Appendix.

$$\begin{aligned}
&\rho C_p\left\{\frac{\partial T}{\partial t}-\frac{1}{J}\left(z_\eta T_\xi - z_\xi T_\eta\right)\frac{\partial r}{\partial t}\right.\\
&\qquad\left.-\frac{1}{J}\left(-r_\eta T_\xi + r_\xi T_\eta\right)\frac{\partial z}{\partial t}\right\}\\
&\qquad -\rho C_p \frac{1}{r}\frac{1}{J}\left(\psi_\xi T_\eta - \psi_\eta T_\xi\right), \qquad (1)\\
&=\kappa\frac{1}{J^2}\left(\alpha T_{\xi\xi} - 2\beta T_{\xi\eta} + \gamma T_{\eta\eta}\right)\\
&\qquad +\kappa\frac{1}{r}\frac{1}{J}\left(z_\eta T_\xi - z_\xi T_\eta\right)
\end{aligned}$$

$$\begin{aligned}
&\frac{\partial C_L}{\partial t}-\frac{1}{J}\left(z_\eta C_{L\xi} - z_\xi C_{L\eta}\right)\frac{\partial r}{\partial t}\\
&\qquad -\frac{1}{J}\left(-r_\eta C_{L\xi} + r_\xi C_{L\eta}\right)\frac{\partial z}{\partial t}\\
&\qquad -\frac{1}{r}\frac{1}{J}\left(\psi_\xi C_{L\eta} - \psi_\eta C_{L\xi}\right), \qquad (2)\\
&=D_L\frac{1}{J^2}\left(\alpha C_{L\xi\xi} - 2\beta C_{L\xi\eta} + \gamma C_{L\eta\eta}\right)\\
&\qquad +D_L\frac{1}{r}\frac{1}{J}\left(z_\eta C_{L\xi} - z_\xi C_{L\eta}\right)
\end{aligned}$$

$$\begin{aligned}
&\frac{\partial C_S}{\partial t}-\frac{1}{J}\left(z_\eta C_{S\xi} - z_\xi C_{S\eta}\right)\frac{\partial r}{\partial t}\\
&\qquad -\frac{1}{J}\left(-r_\eta C_{S\xi} + r_\xi C_{S\eta}\right)\frac{\partial z}{\partial t}\\
&=D_S\frac{1}{J^2}\left(\alpha C_{S\xi\xi} - 2\beta C_{S\xi\eta} + \gamma C_{S\eta\eta}\right), \qquad (3)\\
&\qquad +D_S\frac{1}{r}\frac{1}{J}\left(z_\eta C_{S\xi} - z_\xi C_{S\eta}\right)
\end{aligned}$$

$$\begin{aligned}
&\frac{\partial \omega}{\partial t}-\frac{1}{J}\left(z_\eta \omega_\xi - z_\xi \omega_\eta\right)\frac{\partial r}{\partial t}\\
&\qquad -\frac{1}{J}\left(r_\eta \omega_\xi - r_\xi \omega_\eta\right)\frac{\partial z}{\partial t}\\
&\qquad +\frac{1}{r}\frac{1}{J^2}\left(-r_\eta \psi_\xi + r_\xi \psi_\eta\right)\\
&\qquad \cdot\left(z_\eta \omega_\xi - z_\xi \omega_\eta\right)\\
&\qquad -\frac{1}{r}\frac{1}{J^2}\left(z_\eta \psi_\xi - z_\xi \psi_\eta\right)\\
&\qquad \cdot\left(-r_\eta \omega_\xi + r_\xi \omega_\eta\right)\\
&\qquad -\frac{1}{r^2}\frac{1}{J}\omega\left(-r_\eta \psi_\xi + r_\xi \psi_\eta\right)\\
&=\nu\frac{1}{J^2}\left(\alpha\omega_{\xi\xi} - 2\beta\omega_{\xi\eta} + \gamma\omega_{\eta\eta}\right)\\
&\qquad +\nu\frac{1}{r}\frac{1}{J}\left(z_\eta \omega_\xi - z_\xi \omega_\eta\right)\\
&\qquad -\nu\frac{1}{r^2}\omega\\
&\qquad +\frac{1}{J}Bg\left(z_\eta T_\xi - z_\xi T_\eta\right)\\
&\qquad +\frac{1}{J}Gg\left(z_\eta C_\xi - z_\xi C_\eta\right)
\end{aligned}, \qquad (4)$$

$$\begin{aligned}
&-rJ^2\omega\\
&=\alpha\psi_{\xi\xi} - 2\beta\psi_{\xi\eta} + \gamma\psi_{\eta\eta}\\
&\qquad -\frac{J}{r}\left(z_\eta \psi_\xi - z_\xi \psi_\eta\right)
\end{aligned}, \qquad (5)$$

$$\begin{aligned}
&L_{SL}\rho\frac{\partial f}{\partial t}\\
&=-\kappa_L\frac{1}{r_\xi}\frac{1}{J_L}\left(-\beta T_\xi + \gamma T_\eta\right)_L\\
&\qquad +\kappa_S\frac{1}{r_\xi}\frac{1}{J_S}\left(-\beta T_\xi + \gamma T_\eta\right)_S
\end{aligned}, \qquad (6)$$

$$\begin{aligned}
&\left(C_L - C_S\right)\frac{\partial f}{\partial t}\\
&=-D_L\frac{1}{r_\xi}\frac{1}{J_L}\left(-\beta C_{L\xi} + \gamma C_{L\eta}\right)_L
\end{aligned}, \qquad (7)$$

where, ξ and η are the computational coordinates corresponding to r and z in the physical space, ψ the stream function, ω vorticity, T temperature, ρ density, C_p specific heat, κ thermal conductivity, ν kinetic viscosity, L_{SL} latent heat, B thermal volume expansion coefficient, G the buoyancy coefficient by

the specific gravity difference, g gravity, t time, C the concentration, D the diffusion coefficient. Subscripts of L and S indicate the liquid side and the solid side, respectively. In this study, the governing equations are expressed by using the cylindrical coordinates so as to match the typical flight sample shape.

Calculation Results

(1) One-dimensionality investigation

The prototype cartridge being described in the IAO proposal is shown in Fig. 1. Although we had considered the sample diameter as 20 mm before the IAO proposal, we changed the diameter to 10 mm from the viewpoint of the one-dimensionality. The one-dimensionality, however, is not investigated enough at the proposal. Therefore we began to investigate whether 10 mm diameter sufficiently satisfies the one-dimensionality under the microgravity condition. Since a heat sink diameter might affects on the one-dimensionality, we first investigated the optimal diameter. We know around half of the sample diameter is optimal in the case of the sample of 20 mm in diameter from the results of the past analysis. Thus the cases of 5 mm, 7 mm, 8 mm and 9 mm in diameter were investigated in this analysis. As described in Appendix, the BFC method generates a grid automatically. Therefore the generated grid is shown in Fig. 2.

The boundary conditions are as follows; (i) temperatures on both the cartridge surface and on the end surface at the lower temperature side are given, and (ii) the end surface at the higher temperature side is adiabatic. The given temperature profile on the cartridge surface is the combination of two linear temperature distributions, which brings the best solid-liquid interface shape in the past analysis in the case of the 20 mm-diameter sample.

In order to carry out the calculation, thermophysical properties are required. We summarize these properties as shown in Table 1 and 2. One example of temperature profiles is shown in Fig. 3. Figure 3 (a) is the temperature profiles in the whole region and (b) is the profiles around the molten zone.

In the cases of the heat sink diameters of 5, 7, 8, 9 mm are shown in Figs. 4 – 7. From these results, it is found that all of the interface shapes and the locations are very similar to each other. This means that the heat sink of 5mm or more in diameter can effectively work. Therefore we select 5 mm as the optimal heat sink diameter in this study.

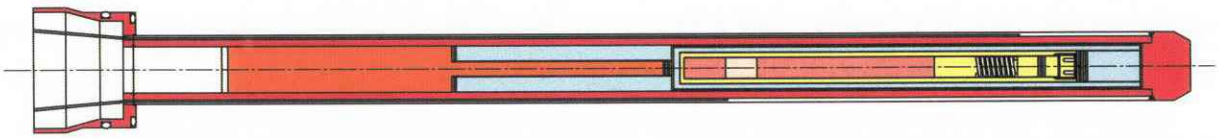

Fig. 1 Schematic View of a Prototype Cartridge

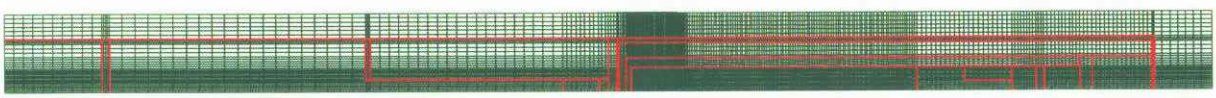

Fig. 2 Generated grid

Table 1 Thermophysical Properties of InGaAs

Coefficient of Volume Expansion β [1/K]	1.83×10^{-4} (GaAs)
Kinetic Viscosity ν [m^2/s]	1.5×10^{-7}
Density of Liquid ρ_L [kg/m^3]	5.9×10^{3} (1296 K)
Density of Solid ρ_S [kg/m^3]	5.3×10^{3} (1296 K)
Viscosity $\mu = \nu \cdot \rho$ [Pa s]	8.9×10^{-4}
Specific Heat C_p [J/(kg K)]	3.2×10^{2} (1296 K)
Thermal Conductivity of Liquid κ_L [W/(m K)]	3.0 (1296 K)
Thermal Conductivity of Solid κ_S [W/(m K)]	1.2 (1296 K)
Thermal Diffusivity of Liquid $\alpha_L = \kappa_L/(\rho_L C_p)$ [m^2/s]	1.6×10^{-6} (1296 K)
Thermal Diffusivity of Liquid $\alpha_S = \kappa_S/(\rho_S C_p)$ [m^2/s]	7.1×10^{-7} (1296 K)
Diffusion Coefficent D_L [m^2/s]	1.0×10^{-8}
Diffusion Coefficent D_S [m^2/s]	1.0×10^{-11}
Latent Heat L_{SL} [J/kg]	5.0×10^{5}

Table 2 Typical Thermophysical Properties

Material	Thermal Conductivity κ [W/(m K)]	Density ρ [kg/m^3]	Specific Heat C_p [J/(kg K)]
Ta	60.2	16.36×10^{3}	1.54×10^{2}
WC-103	38.1 (1144 K) 40.7 (1386 K)	8.85×10^{3}	3.43×10^{2}
Cu	3.5×10^{2}	8.96×10^{3}	5.0×10^{2}
Fused Crystal	4.0	2.2×10^{3}	1.13×10^{3}
BN / pBN	7.0	2.0×10^{3} (BN) 2.1×10^{3} (pBN)	2.1×10^{3}
Carbon Cloth / Laminated Carbon Sheet	5.0	1.0×10^{3}	1.68×10^{3}
Graphite Spring	44.0	1.7×10^{3}	1.68×10^{3}
Arsenic Vapor (1 atm)	1.58×10^{-3}	1.45	1.0×10^{3}
Vacuum ($\sim 10^{-5}$ Torr)	9.2×10^{-11}	3.7×10^{-10}	1.01×10^{3}

In the case of the 5mm-diameter heat sink, composition, temperature and temperature gradient along the interfaces are investigated as shown in Figs. 8 – 10. These figures show that the radial difference at the growth interface is within about ±1 %. Here, we define that the radial difference is the percentage of the difference between the maximal value and the minimal one to the minimum along the interface. For example, in Fig. 8 (a), the minimum is about 0.2883 and the maximum is about 0.2890, thus the radial difference is about 0.24 %. Namely, the one-dimensionality is sufficiently satisfied under the microgravity condition. On the other hand, the radial difference at the feed interface is relatively large as compared with the difference at the growth interface. Especially, the radial difference of the temperature gradient at the feed side is about ±30 %. This means that the one-dimensionality at the feed side is broken in the case of the 10 mm-diameter sample.

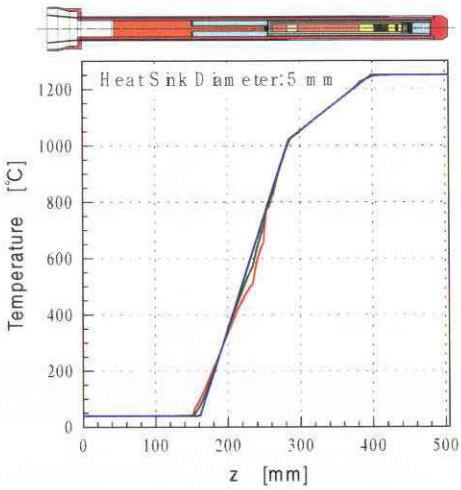

(a) Temperature Profiles in Whole Region

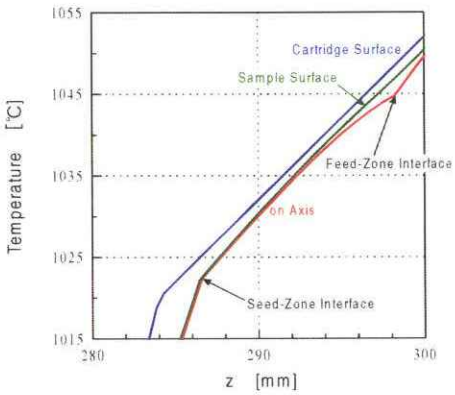

(b) Temperature Profiles around Zone

Fig. 3 Schematic View of a Cartridge

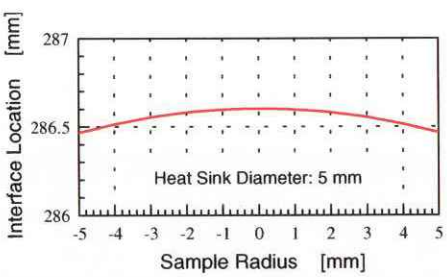

(a) Growth Interface

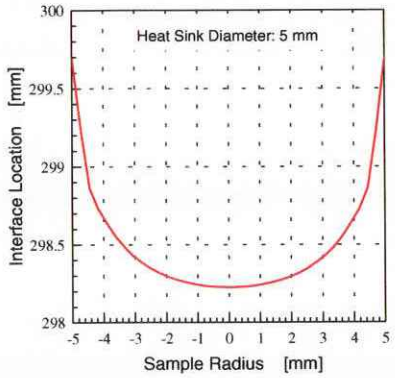

(b) Feed Interface

Fig. 4 Interface Shape and Location (5 mm)

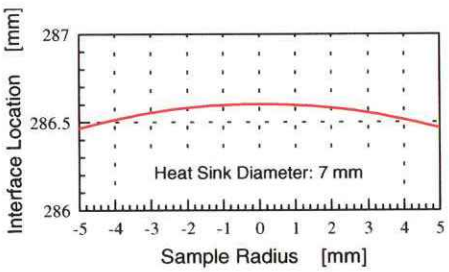

(a) Growth Interface

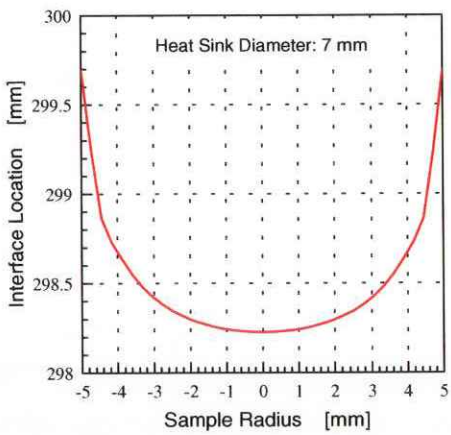

(b) Feed Interface

Fig. 5 Interface Shape and Location (7 mm)

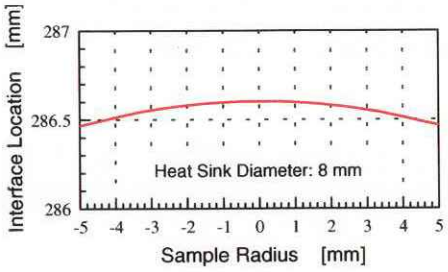

(a) Growth Interface

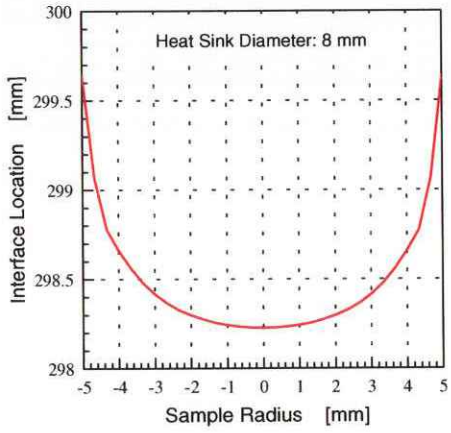

(b) Feed Interface

Fig. 6 Interface Shape and Location (8 mm)

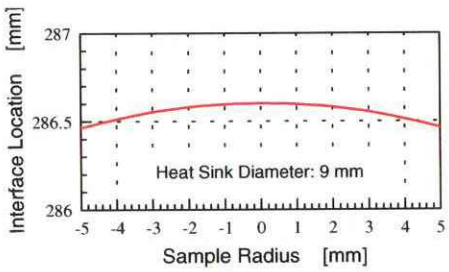

(a) Growth Interface

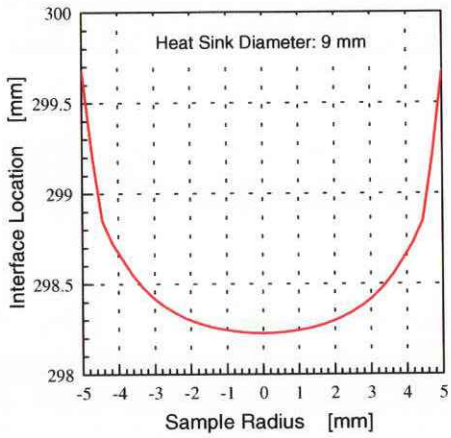

(b) Feed Interface

Fig. 7 Interface Shape and Location (5 mm)

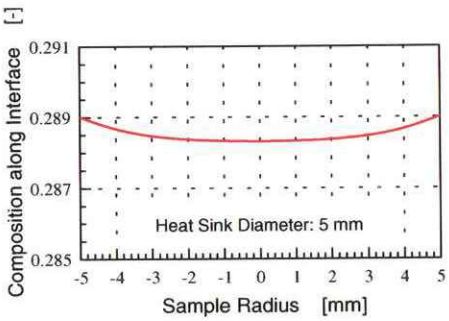

(a) Growth Interface

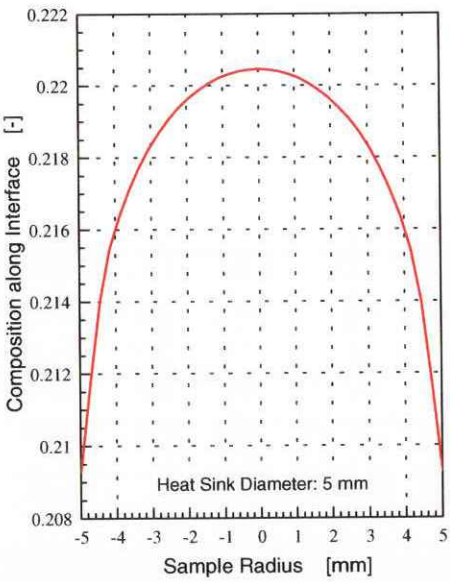

(b) Feed Interface

Fig. 8 Composition along Interface

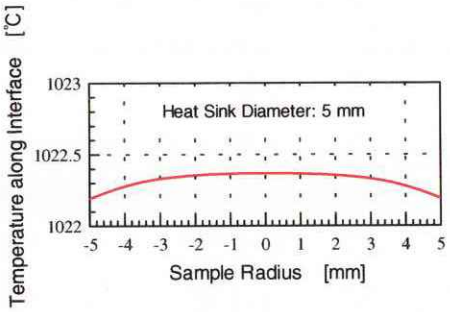

(a) Growth Interface

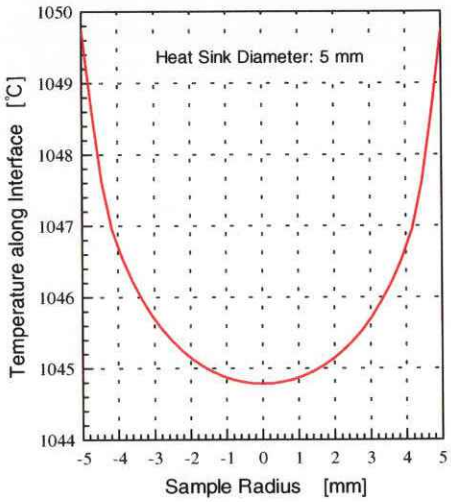

(b) Feed Interface

Fig. 9 Temperature along Interface

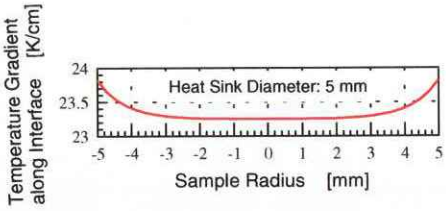

(a) Growth Interface

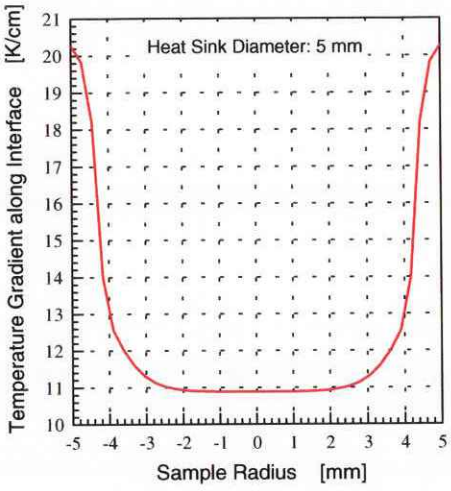

(b) Feed Interface

Fig. 10 Temperature Gradient along Interface

(2) Design of dummy ampoule

The reliability of the numerical analysis has been verified in each development phase. We have confirmed that the numerical code is sufficiently reliable in the case of the melt growth such as the Bridgeman method. But the reliability in the case of the TLZ method has not been verified yet. In the melt growth, the mass transport was not programmed. Therefore, we have planned to verify the reliability of the current code.

In order to verify the code, the temperature distribution inside the ampoule, which is compared with the numerical result, must be measured. Although any ampoule configuration is basically acceptable to acquire the temperature data, the configuration being similar to the flight cartridge is much convenient as compared with any other configurations. Therefore we decided to design a cartridge that is similar to the prototype flight cartridge shown in Fig. 1.

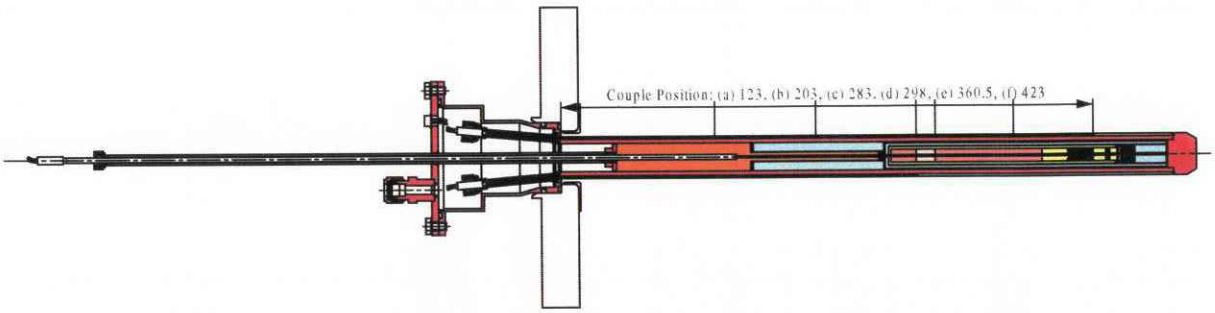

Fig. 11 Dummy Cartridge

The cartridge used for the temperature measurement, which is based on the flight cartridge, is usually called a dummy cartridge. The dummy cartridge is used for not only reliability verification but also optimization of furnace parameters.

By using the heat sink diameter of 5 mm, the dummy cartridge is designed as shown in Fig. 11. The dummy cartridge has several features, that is, (i) six fixed thermocouples are installed on the cartridge surface, (ii) one movable thermocouple is installed into the axis, (iii) gas can be confined inside the cartridge, and (iv) dummy sample is changeable.

The fixed thermocouples on the cartridge surface are provided for obtaining the temperature profile on the surface. The profile is used as the temperature boundary conditions on the surface in the numerical analysis.

The movable thermocouple is used for obtaining the temperature profile in the axial direction. The profile is compared with the numerical result in order to verify the reliability. Of course, both temperature data are also used for the optimization of the furnace parameters in future.

The gas environment can drastically improve the thermal conduction between two materials. Therefore, we can neglect the effect of the point contact on the thermal conduction. In addition, the reproducibility of the cartridge performance is also much improved even though a component inside the cartridge is exchanged to a new one.

The dummy sample can be exchanged to other samples. Therefore, if the dummy sample is exchanged to an InGaAs sample, a preliminary experiment can be carried out.

As mentioned above, the dummy cartridge has several advantages, but the cartridge has a potentially weak point. That is the interface part called the boss section. The boss section differs from that of the standard cartridge. In the standard dummy cartridge, the boss is fixed on the flange by using a metal fitting. In our dummy cartridge, it is difficult to design the interface to the fitting due to the large size of the boss section. Therefore, in the present plan, the cartridge is fixed on the flange by utilizing the pressure difference between atmospheric pressure and the chamber pressure of the vacuum. In the vertical configuration, it is expected that the airtight can be maintained by the pressure difference. But if it does not work as we expect, the boss section must be modified in order to attach the fitting. Adding such function is not so easy work, but can be achieved by using a larger boss section from the preliminary investigation result of the modification.

(3) Convection influence in 2 mm sample

At the proposal, we believed that the microgravity environments were required in order to

satisfy the one-dimensionality. Recently, however, we began to consider that a capillary tube might sufficiently reduce the convection influence on some important phenomena such as thermal transport and mass transport.

The self-consistent numerical analysis, which is used for getting solutions shown in the one-dimensionality analysis, can give us more precise solutions but needs a long time, for example, more than one month per one analysis. We had only about one year before the candidates for flight experiments were in public. Of course, if our experiment is selected as the candidate, we have to clearly explain the need for microgravity. The need for microgravity is directly coupled with both the experimental plan such as the number of the samples and the operational plan such as the assignments of the ISS resources.

The numerical analysis was carried out in the case of the zone model. The zone model consists of the only one cylindrical region as shown in Fig. 12. The thermophysical properties in this region are those of the InGaAs melt. Since the boundary conditions at the top and at the bottom are difficult, we investigate the dependence of the Sherwood number on the temperature difference between the center axis and the edge. The Sherwood number Sh is defined as

$$Sh=\frac{hL}{D}, \tag{8}$$

where h is the mass transfer coefficient, L the system length, D the diffusion coefficient. Now we assume the dimension can be considered one-dimensional. This assumption is described as

$$-D\frac{\partial C}{\partial z}+Cv=h\Delta C, \tag{9}$$

where C is the concentration, v the flow rate, ΔC is the concentration difference between the concentration at $z=0$ and that at $z=L$. Since we assume the InGaAs melt is the incompressible fluid, v must be equal to 0 at the wall such as the interface. Therefore, Eq. (9) can be rewritten as

$$h=\left.-D\frac{\partial C}{\partial z}\right/\Delta C. \tag{10}$$

By substituting Eq. (10) to Eq. (8), we obtain the Sherwood number as

$$Sh=\left.-\frac{\partial C}{\partial z}\right/\frac{\Delta C}{L}. \tag{11}$$

This means that the Sherwood number is the ratio of the concentration gradient at the interface to the slope of the line connected between the concentrations at $z=0$ and at $z=L$. By using Eq. (11) and the numerically obtained concentration distribution data, we can calculate the local Sherwood number at each radius. In the numerical analysis, we use the following boundary conditions, that is, (i) the linear temperature profile is given on the cylindrical surface, (ii) the linear temperature profile or the adiabatic condition is given at the end surface, and (iii) the concentration corresponding to the temperature is given at the end surface. Although the radial temperature difference between the center and the surface is the main driving force of the convection, we cannot know the actual temperature difference. Hence, we varied the temperature difference as a parameter, and investigated the maximum allowable difference that can neglect convection influence.

By radially averaging the local Sherwood number, which is calculated by using the numerically

obtained concentration data, the averaged Sherwood number is obtained. The averaged Sherwood number represents the enhancement of the mass transport from one interface to the other interface by the convection. In the case of the averaged Sherwood number being equal to 1, the mass is transported only by the diffusion and thus the numerator is equal to the denominator in Eq. (11). This is exactly the same as the solution of the diffusion equation.

We calculate the averaged Sherwood number, however, the number is almost 1. This means that the mass transport by the diffusion is dominant in this case. This suggests that 2mm-diameter sample can satisfy the one-dimensionality. But we need more accurate investigation in this case. More detailed discussion is described in the later section.

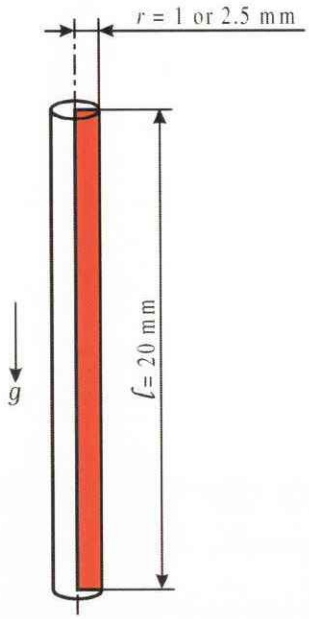

Fig. 12 Zone Model

(4) Updated thermophysical properties

Since the thermal conductivity of InGaAs is unknown, we used the estimated values of these of the solid and the liquid in all of the numerical analyses mentioned above. The ratio of the conductivity of 2.5, that of the liquid κ_L to that of the solid κ_S, was used. The ratio is one of the most important values because the temperature gradient at the interface is basically determined by this ratio. Therefore we have tried to measure the thermal conductivity. By using a laser flash method, we succeeded in measuring the thermal diffusivity at the end of this year. From the measurement result, we found that the diffusivity ratio is about 6. This is unexpected result and the impact on the numerical analysis was large. Thus we updated the thermophysical properties and investigated the difference between the older results and the updated results. Unfortunately, only the thermal diffusivity has been obtained. Therefore, we have to estimate the thermal conductivity and the specific heat. We use the specific heat of GaAs as that of InGaAs, and then we calculate the thermal conductivity by using the thermal diffusivity, the specific heat and the density. Finally we obtain the ratio of the thermal conductivity and the ratio is more than 7. The updated properties that currently we use are summarized in Table 3. In addition, we revised other properties. These properties are also summarized in Table 4. The major change is the properties of BN.

Table 3 Updated Thermophysical Properties of InGaAs (Cont.)

Coefficient of Volume Expansion β [1/K]	9.34×10^{-5}
Coefficient of Specific Gravity Change γ [1/mol]	-1.85×10^{-1}
Kinetic Viscosity ν [m^2/s]	1.5×10^{-7}
Density of Liquid ρ_L [kg/m^3]	5.9×10^{3}
Density of Solid ρ_S [kg/m^3]	5.3×10^{3}
Viscosity $\mu = \nu \cdot \rho$ [Pa·s]	8.9×10^{-4}

Table 3 Updated Thermophysical Properties of InGaAs

Specific Heat of Liquid C_{pL} [J/(kg·K)]	3.5×10^{2}
Specific Heat of Solid C_{pS} [J/(kg·K)]	3.2×10^{2}
Thermal Conductivity of Liquid κ_L [W/(m·K)]	22.7
Thermal Conductivity of Solid κ_S [W/(m·K)]	3.0
Thermal Diffusivity of Liquid $\alpha_L = \kappa_L/(\rho_L \cdot C_p)$ [m^2/s]	1.1×10^{-5}
Thermal Diffusivity of Liquid $\alpha_S = \kappa_S/(\rho_S \cdot C_p)$ [m^2/s]	1.8×10^{-6}
Diffusion Coefficent D_L [m^2/s]	1.0×10^{-8}
Diffusion Coefficent D_S [m^2/s]	1.0×10^{-11}
Latent Heat L_{SL} [J/kg]	5.0×10^{5}

Table 4 Revised Typical Thermophysical Properties

Material	Thermal Conductivity κ [W/(m·K)]	Density ρ [kg/m^3]	Specific Heat C_p [J/(kg·K)]
Ta	60.2	16.36×10^{3}	1.54×10^{2}
WC-103	38.1 (1144 K) 40.7 (1386 K)	8.85×10^{3}	3.43×10^{2}
Cu	3.5×10^{2}	8.96×10^{3}	5.0×10^{2}
Fused Crystal	4.0	2.2×10^{3}	1.13×10^{3}
BN / pBN	23.7	1.8×10^{3} (BN) 2.1×10^{3} (pBN)	1.881×10^{3}
Carbon Cloth / Laminated Carbon Sheet	5.0	1.0×10^{3}	1.68×10^{3}
Graphite Spring	44.0	1.7×10^{3}	1.68×10^{3}
Arsenic Vapor (1 atm)	1.58×10^{-3}	1.45	1.0×10^{3}
Vacuum (~ 10^{-5} Torr)	9.2×10^{-11}	3.7×10^{-10}	1.01×10^{3}

We investigated the differences of several results between in the case of the older properties and in the case of the updated ones. The typical result of the temperature profile is shown in Fig. 13. In this case, the combination of the two linear temperature profiles are used as the temperature boundary condition on the cartridge, that is, the same boundary condition as Figs. 3 and 4. Figure 3 (b) is shown again in Fig. 13 (b), though the scale is changed, to make the comparison more easily. By comparing these results, it is found that the profiles of the sample are quite different. In the old properties case, the profiles are convex towards the top and are almost parallel to the profile on the cartridge surface. On the other hand, in the updated case, the profiles are not parallel to it and the profile on axis is S-shape in the zone. This is mainly caused by the change of the ratio of the thermal conductivity from 2.5 to more than 7.

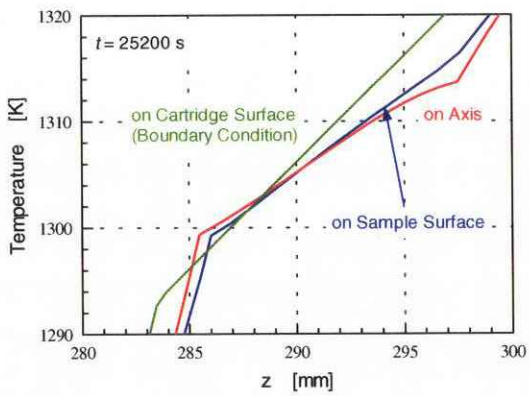

(a) Updated Properties Case

Fig. 13 Typical Results of Temperature Profiles (Cont.)

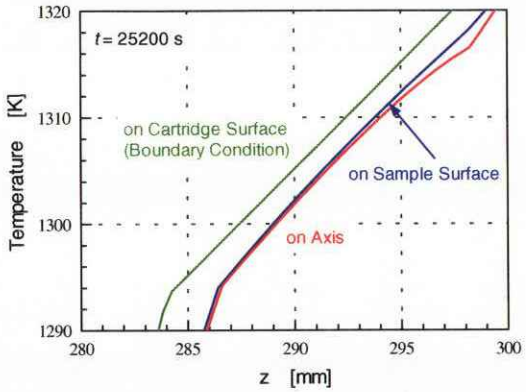

(b) Old Properties Case

Fig. 13 Typical Results of Temperature Profiles

The changes of the interface shapes are also investigated and are shown in Fig. 14. As shown in Fig. 14, the change at the feed side is relatively small but the change at the growth interface is drastic. Especially, the shape changes from the convex shape to the concave shape towards the melt. This shape must be improved in order to grow a single crystal. The improvement of the interface shape will be investigated in near future after completion of the verification of the one-dimensional model.

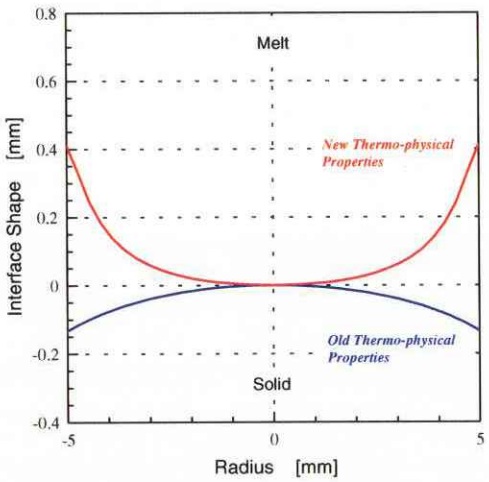

(a) Growth Side

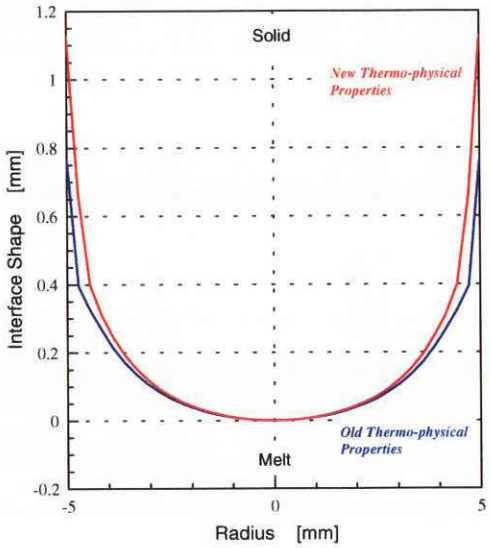

(b) Feed Side

Fig. 14 Comparisons of Interface Shapes

Discussion

As described in the result section, the one-dimensionality is satisfied at the growth interface in the case of the sample diameter of 10 mm. But at the feed side, the one-dimensionality is broken in this case. So we may have to investigate the sample diameter satisfying the one-dimensionality. But we do not deeply understand the characteristics of the 10 mm-diameter samples. For example, the temperature profile given on the cartridge surface is ideal, i.e., the combination of two lines, though that should be like a parabolic curve such as the second order or the fourth order in the actual experiments. Therefore we investigate the one-dimensionality in the cases of several types of the polynomial curves before we investigate other samples with different diameters.

Thus we carried out the numerical analysis by using the temperature boundary condition of the polynomial curves on the cartridge surface, but all the attempts to achieve the one-dimensionality at the feed side were failed. In addition, the one-dimensionality at the growth side went worse.

Therefore, we have to consider samples with a smaller diameter even though under the microgravity conditions. We will try to solve this problem next year.

The reason why the one-dimensionality is required is originated from the one-dimensional model that should be verified as mentioned previously. The one-dimensional model is first described in the proposal to the IAO. In the proposal, the one-dimensional model was described as

$$V = -\frac{D}{C_L - C_S}\left.\frac{\partial C}{\partial T}\right|_{int}\left.\frac{\partial T}{\partial z}\right|_{int}, \qquad (12)$$

where V is the spontaneous growth rate, the differential of the first term is the reciprocal of the slope of the tangential line to the liquidus, and the differential of the second term is the temperature gradient. This equation indicates that the growth rate is controlled not by the concentration gradient but by the temperature gradient.

In order to describe the growth rate as Eq. (12), we create the new concept of the solution growth, that is, the concentration in the liquid is saturated at the concentration determined by the liquidus curve. This is the origin of the name of the TLZ method. This concept is innovative because both the concentration and the growth rate are controlled by the only temperature profile. Namely, the TLZ method is the melt-growth-like solution growth. This is the crucially different point as compared with the other solution growth techniques.

Of course, the model is applicable to the calculations of both the growth rate and the dissolution rate at the growth interface and at the feed interface. Equation (12) indicates that any parameters at the other interface are not required to calculate the rate at one interface. This is the practically useful feature of the TLZ method.

To calculate Eq. (12), we must know the values of C_L, C_S, the temperature and the temperature gradient. Here, we introduce an assumption of quasi-equilibrium at the interface, that is, there are no supersaturation and no supercooling at the interface. Therefore, if we can know the temperature at the interface, we can obtain both C_L and C_S from the phase diagram.

The residual unknown parameter is the temperature gradient. So we establish a new method of estimating the temperature gradient. This method has no name yet but we call it "Nakamura's method" in this paper for convenience. Dr. Nakamura is the person who established the new estimation method [10].

In the Nakamura's method, a linear temperature profile inside the melt is assumed. From this assumption, the temperature gradient can be estimated by connecting the temperatures corresponding to the solid compositions at both interfaces. In the present sample configuration, however, the melting point of the feed is set higher than the environmental temperature to prevent from being molten. Therefore we form the solid-liquid two-phase coexistence region near the feed interface in order to obtain the equilibrium solid composition near the feed interface. After obtaining the solid compositions at both interfaces, the corresponding solidus temperatures can be obtained. From the slope of the line connected the two solidus temperatures, we can obtain the temperature gradient. This is the outline of the Nakamura's method.

By using the Nakamura's method, the growth rate in Eq. (12) can be estimated. The accuracy of this estimation is determined by the linearity of the temperature profile in the liquid. In fact, the estimated growth rate matches with the actual

averaged growth rate in some experiments but does not match in other experiments. Therefore the linearity should be investigated.

In order to know the temperature profile in the melt, we apply the model based on the configuration shown in Fig. 1 to the analysis. To match the model with the actual configuration as much as possible, the sample diameter is changed from 10 mm to 2 mm because the 2 mm-diameter sample is used in the ground-based experiment. In addition, the gravity of 1 g is used in this analysis.

The result is shown in Fig. 15. As shown in Fig. 15, we can obtain three types of the temperature gradients, that is, the environment, the slope of the line connected between the temperature at both the interfaces, and the slope of the line being tangential to the calculated temperature profile. These gradients are 10 K/cm, 7.9 K/cm and 2.9 K/cm, respectively. The gradient of 2.9 K/cm is about 30 % of the environmental gradient. In addition, this gradient is about 36 % of the gradient from the connected line between the temperatures at the interfaces. This value is much smaller than that obtained from Nakamura's method. We initially expected that the gradient at the interface was close to the slope of the connected line.

Unfortunately, the slope of the connected line is closer to the environment, that is, about 80 % of the environment. This numerical analysis indicates that the Nakamura's method brings the overestimated growth rate. This should be the reason why the actual growth rate does not match with the estimated one in some experiments. But in other experiments, the estimated value well matches the actual one. The reason is now under investigation and will be clarified next year, but now we consider that difference of the thermal conduction should be the main reason. We use the InGaAs seed in some experiments, and the GaAs seed in other experiments. If the thermal conductivity of the InGaAs seed is far different from that of the GaAs seed, the temperature profile in the InGaAs case is drastically different from that in the GaAs case as a natural result. Figure 13 is one of the good examples. In Fig. 13, (a) is obtained in the case of the thermal conductivity ratio of the melt to the solid is more than 7, and (b) in the case of the ratio of 2.5. Under the quasi-steady state condition, the temperature profile is dominated by the thermal conductivity ratio at the boundary.

We will concentrate on this problem in 2002 because this must be solved from the viewpoint of the model verification. In addition, in order to carry out more precise analysis, we will provide a new model based on the ground-based experiments in 2002.

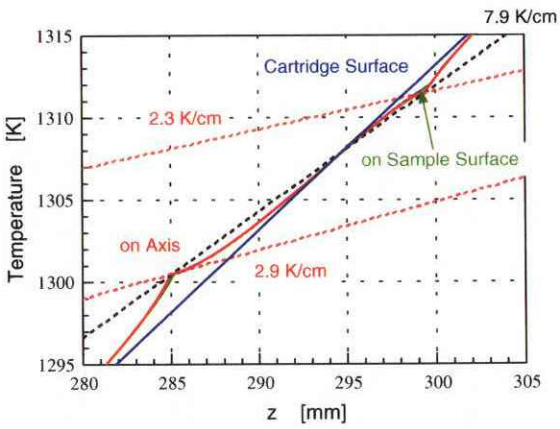

Fig. 15 Temperature Profiles (ϕ 2 Sample)

By using the temperature distributions, heat fluxes can be calculated. The heat flux is the boundary condition of the numerical analysis that has been carried out by the team member belonging to Toyo University. Although the heat flux may be the better boundary condition as compared with the fixed temperature boundary condition, it is difficult to find the suitable and realistic heat flux profile. Therefore they need an example of the heat flux

profile to adjust the boundary condition. In order to assist their analysis, we calculate the heat flux profiles from our numerical results. The typical heat flux profiles are shown in Figs. 16 and 17. In Fig. 16, the combination of two linear temperature profiles, e.g. Fig. 3, is used. On the other hand, in Fig. 17, a parabolic temperature profile is used. Although these results are obtained in the case of the old thermophysical properties, these can enhance qualitative understanding of the heat flux profile. These data have been sent to Toyo University and they have been successful in establishing suitable heat flux profiles.

By comparing Fig. 16 (a) with Fig. 17 (a), it is found that the heat flux in Fig. 16 (a) is much smaller than that in Fig. 17 (a) near the growth interface. Since the positive value of the heat flux means the heat loss from the sample, this causes the concave interface shape. If we succeed in reducing the heat loss at the interface, we can obtain the flatter shape. Unfortunately, the loss is determined by the ratio of the thermal resistance of the solid to that of the crucible. Therefore, it is much difficult to reduce the heat loss. We will focus on this problem after verification of the one-dimensional model.

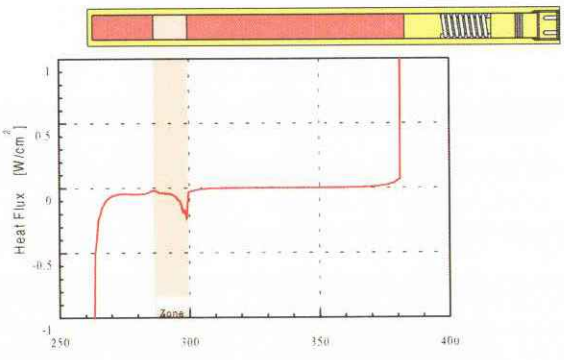

(a) On sample surface

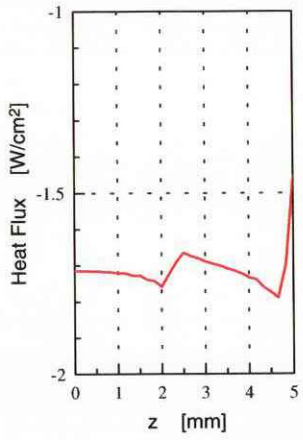

(b) On end surface at lower temperature side

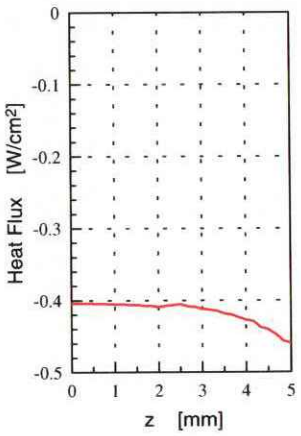

(c) On end surface at higher temperature side

Fig. 16 Heat Flux Profiles (Linear Temperature)

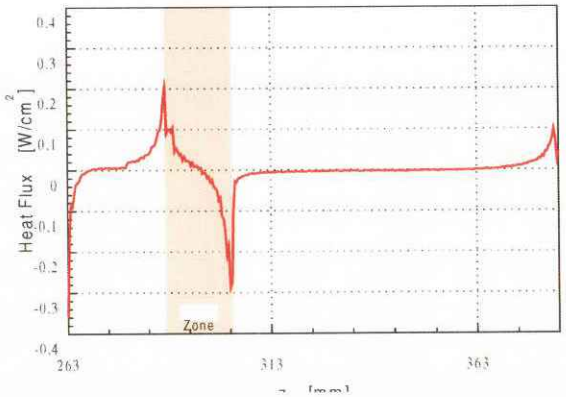

(a) On sample surface

Fig. 17 Heat Flux Profiles (Parabolic Temperature) (Cont.)

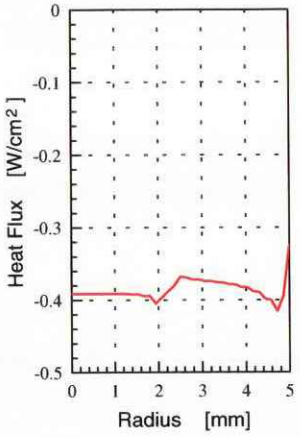

(b) On end surface at lower temperature side

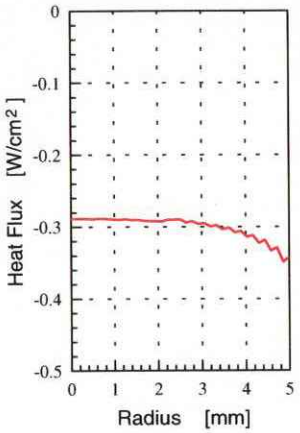

(c) On end surface at higher temperature side

Fig. 17 Heat Flux Profiles (Parabolic Temperature)

We usually expect that the there is one large vortex and flows in the whole region. In such case, the mass is transported by the flow from one interface to the other interface and is consumed at the other interface. As mentioned in the previous section, the averaged Sherwood number is almost 1 in the case of the 2 mm-diameter sample. This usually means that the mass transport from one interface to the other interface is dominated by the diffusion and the convection is negligibly weak.

In order to confirm the convection is negligibly weak, we investigate the flow pattern in the melt. The typical flow pattern is shown in Fig. 18. In Fig. 18, two vortexes exist at the two different locations. This is not the pattern we expect. In this case, the mass is also transported by the convection, but almost all the mass may return to the same interface at the different radial location. If this is true, the convection enhances not the axial mass transport but the radial transport. Therefore, the mass transport may be affected by the convection even though in the case of the 2mm-diameter sample. In addition, if the convection enhances the radial mass transport, the one-dimensionality is broken.

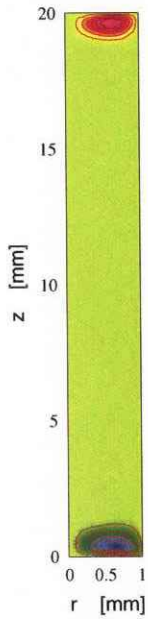

Fig. 18 Typical Flow Pattern

Unfortunately, it is very difficult to calculate the Sherwood number by using the radial distribution of the concentration. Therefore we need another index that can represent the convection influence. Since the Sherwood number is appropriate index representing the convection influence, we begin to revise the expression of the Sherwood number. From Eq. (11), the Sherwood number is rewritten as

$$Sh = \left(-D \left.\frac{\partial C}{\partial z}\right|_{conv} \right) \Big/ \left(-D \left.\frac{\partial C}{\partial z}\right|_{diff} \right), \qquad (13)$$

where the numerator is the mass flux affected by the convection and the denominator is the flux under the pure diffusion condition. Because the numerator is the summation of the mass flux by the diffusion and the flux by the convection, we rewritten the numerator as

$$-D \left.\frac{\partial C}{\partial z}\right|_{conv} = -D \left.\frac{\partial C}{\partial z}\right|_{diff} + A, \qquad (14)$$

where A is the mass flux caused by the convection. By substituting Eq. (14) to Eq. (13), we obtain

$$Sh = 1 + \frac{A}{-D \left.\frac{\partial C}{\partial z}\right|_{diff}}. \qquad (15)$$

Equation (15) indicates that Sh may be smaller than 1 when A is negative. The negative A means that the convection transports the mass in the same direction of the transport by the diffusion. In such case, the convection increases the total mass transport and thus the concentration gradient becomes smaller in order to satisfy the equation of the continuity. On the other hand, the gradient must increase at a certain radius since the flow direction is opposite. Namely, the local Sherwood number varies from less than 1 to more than 1 along the interface. But by averaging the local Sherwood number, the averaged Sherwood number becomes around 1 as mentioned previously. This means that the mass transport by the convection to the other interface is negligibly small but does not mean that the convection influence is negligibly small. The convection enhances the radial mass transport as mentioned above.

In order to discuss the convection effect more quantitatively, we introduce the modified definition of the Sherwood number, that is,

$$C.I.I. = 1 + \frac{|A|}{-D \left.\frac{\partial C}{\partial z}\right|_{diff}}. \qquad (16)$$

Since this is not the Sherwood number, we define this expression as the convection influence index (*C.I.I.*). In the case of Sh being less than 1, the convection effect exists. Therefore we introduce the absolute value of A in order in order to count the convection effect. Thus the *C.I.I.* is always more than 1.

From Eq. (14), A is expressed as

$$A = -D \left.\frac{\partial C}{\partial z}\right|_{conv} - \left(-D \left.\frac{\partial C}{\partial z}\right|_{diff} \right). \qquad (17)$$

By substituting Eq. (17) to Eq. (16), we can obtain the *C.I.I.* as

$$C.I.I. = \begin{cases} Sh & (Sh \geq 1) \\ 2 - Sh & (Sh < 1) \end{cases}. \qquad (18)$$

The *C.I.I.* becomes simple expression and is useful. To evaluate the convection effects, we radially average the *C.I.I.* and show the *C.I.I.* under the various conditions in Figs. 19. These figures shows that if the *C.I.I.* of less than 1.1 is allowable, the temperature difference between the center and the edge must be less than 0.1 K, 0.225 K and 0.45 K in the cases of the temperature gradient of 10 K/cm, 20 K/cm and 40 K/cm, respectively. Therefore, the higher temperature gradient is better in order to improve the one-dimensionality. The one-dimensionality is one of the most important

experimental conditions from the viewpoint of the verification of the one-dimensional model. Therefore we will numerically investigate whether the actual radial temperature difference matches the requirements by applying more precise model next year.

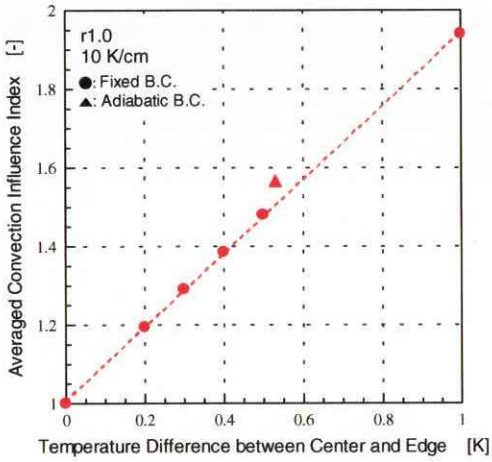

(a) 10 K/cm, r = 1.0 mm

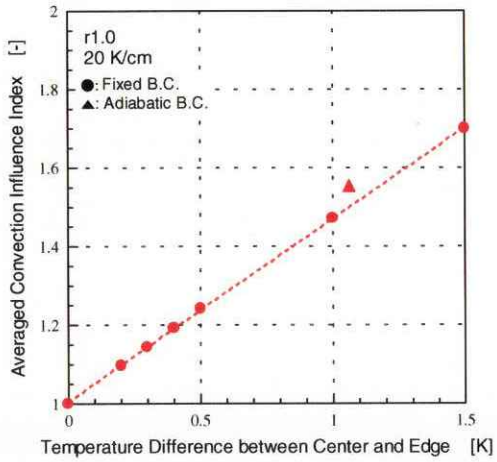

(b) 20 K/cm, r = 1.0 mm

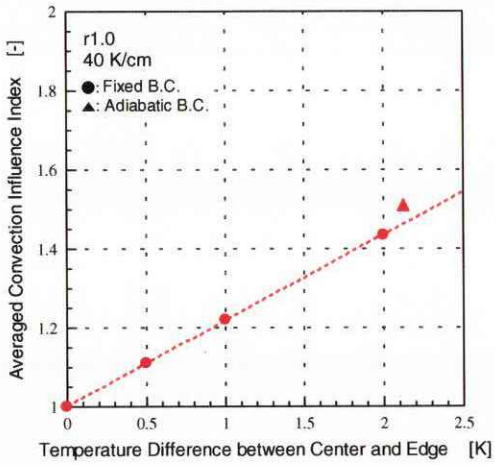

(c) 40 K/cm, r = 1.0 mm

Fig. 19 C.I.I. under Various Conditions

Conclusions

The one-dimensionality at the growth interface was verified by the numerical analysis under the microgravity condition in the case of the sample diameter of 10 mm. But the one-dimensionality at the feed interface was not achieved in this case. By considering the ideal temperature boundary conditions, it may be difficult to improve the one-dimensionality at the feed side any more. A sample diameter better satisfying the one-dimensionality will be investigated next year.

The dummy cartridge has a potentially weak point, i.e., the boss section. We will investigate the interface matching between the boss section and the furnace, based on the engineering model. The fully functional dummy cartridge will be provided in 2002.

The result of the 2 mm sample analysis is obtained by using the model of only the melt zone. This model requires much shorter CPU time as compared with the self-consistent model. The numerical results have enough reliability to understand the convection influence. From the numerical result, it is found that the convection does not enhance the axial mass transport but enhances the

radial mass transport. This means that the one-dimensionality become worse when the flow rate is high. Therefore we investigate the maximum allowable radial temperature difference between the center and the surface. The investigation indicates that the larger temperature gradient brings the better one-dimensionality. Since the one-dimensionality is the most important requirement, we will perform further investigation in 2002. In addition, we are planning to investigate the effects of the non-axisymmetricity such as the off-axis setting or the tilted setting next year.

The thermophysical properties are updated. This update caused the drastic change of the temperature profile inside the melt. By changing from the old properties to the updated properties, the profile changes from the slightly curved line to the gentle S-shape curve. This is the main reason why the temperature gradient inside the melt is so different from the gradient of the environment.

We also investigated the temperature gradient inside the melt. From the result of the numerical analysis, it is found that the gradient inside the melt is less than 30 % of the environmental gradient. This should be the main reason why the estimated growth rate by using the Nakamura's method does not match the actual growth rate in some experiments. In order to carry out more precise analysis, we will provide the new model of the 2 mm-diameter sample next year. The new model will be based on the ampoule used in the ground-based experiment. Since the temperature gradient is directly related to the verification of the one-dimensional model, the model provision and the analysis will be performed as soon as possible.

By using results from the numerical analysis, we calculated the heat flux profiles. These profiles can be used as the example profiles for boundary conditions, which are necessary to the numerical analysis carried out by team members at Toyo University. The profiles have already sent to them and they have succeeded in getting suitable boundary conditions.

Acknowledgement

The authors are thankful to Prof. Maekawa at Toyo Univ. for his valuable advice and discussion.

Appendix

The governing equations in the physical space are the energy transport equation, the mass transport equation, the vorticity transport equation, the stream function equation, the energy balance equation and the mass balance equation. These equations are represented as follows;

$$\rho C_p \frac{\partial T}{\partial t} + \rho C_p \left(\frac{1}{r}\frac{\partial \psi}{\partial z}\frac{\partial T}{\partial r} - \frac{1}{r}\frac{\partial \psi}{\partial r}\frac{\partial T}{\partial z} \right) = \kappa \left(\frac{\partial^2 T}{\partial r^2} + \frac{1}{r}\frac{\partial T}{\partial r} + \frac{\partial^2 T}{\partial z^2} \right), \quad \text{(A-1)}$$

$$\frac{\partial C_i}{\partial t} + \left(\frac{1}{r}\frac{\partial \psi}{\partial z}\frac{\partial C_i}{\partial r} - \frac{1}{r}\frac{\partial \psi}{\partial r}\frac{\partial C_i}{\partial z} \right) = D_i \left(\frac{\partial^2 C_i}{\partial r^2} + \frac{1}{r}\frac{\partial C_i}{\partial r} + \frac{\partial^2 C_i}{\partial z^2} \right), \quad (i = S \text{ or } L), \quad \text{(A-2)}$$

$$\frac{\partial \omega}{\partial t} + \frac{1}{r}\frac{\partial \psi}{\partial z}\frac{\partial \omega}{\partial r} - \frac{1}{r}\frac{\partial \psi}{\partial r}\frac{\partial \omega}{\partial z} - \frac{1}{r^2}\omega\frac{\partial \psi}{\partial z} = \nu \left(\frac{\partial^2 \omega}{\partial r^2} + \frac{1}{r}\frac{\partial \omega}{\partial r} + \frac{\partial^2 \omega}{\partial z^2} - \frac{1}{r^2}\omega \right) + B g \frac{\partial T}{\partial r} + G g \frac{\partial C_L}{\partial r}, \quad \text{(A-3)}$$

$$-r\omega = \frac{\partial^2 \psi}{\partial r^2} - \frac{1}{r}\frac{\partial \psi}{\partial r} + \frac{\partial^2 \psi}{\partial z^2}\ , \qquad \text{(A-4)}$$

$$L_{SL}\ \rho\, \boldsymbol{u}\cdot\hat{\boldsymbol{n}} = -\kappa_L \left(\frac{\partial T}{\partial n}\right)_L + \kappa_S \left(\frac{\partial T}{\partial n}\right)_S\ , \text{and} \qquad \text{(A-5)}$$

$$\left(C_L - C_S\right)\boldsymbol{u}\cdot\hat{\boldsymbol{n}} = -D_L \left(\frac{\partial C_L}{\partial n}\right)_L\ , \qquad \text{(A-6)}$$

where, ψ is the stream function, ω vorticity, T temperature, ρ density, C_p specific heat, κ thermal conductivity, ν kinetic viscosity, L_{SL} latent heat, B thermal volume expansion coefficient, G the buoyancy coefficient by the specific gravity difference, g gravity, r radius, z length, t time, C the concentration, $\boldsymbol{u}$ moving velocity vector of the interface, $\hat{\boldsymbol{n}}$ normal unit vector to the interface, D the diffusion coefficient. Subscripts of L and S indicate the liquid side and the solid side, respectively. In this study, the governing equations are expressed by using the cylindrical coordinates so as to match a typical flight sample shape.

In order to obtain temperatures and concentrations in the liquid and the solid at the interface, Eqs. (A-5) and (A-6) are solved simultaneously. In Eqs. (A-5) and (A-6), however, there are three variables. Therefore additional relationship is required. In this study, a phase diagram is used as the additional relationship. By using the phase diagram of InGaAs [11] as shown in Fig. A-1, the relationships between the concentration in the solid and the temperature, and between the concentration in the liquid and the temperature can be described as

$$C_S = f_S(T)\ , \text{and} \qquad \text{(A-7)}$$

$$C_L = f_L(T)\ , \qquad \text{(A-8)}$$

where f_S and f_L represent the solidus and the liquidus. Figure A-1 is an inverse plot as compared with a usual plot, that is, the horizontal and the vertical axes are exchanged.

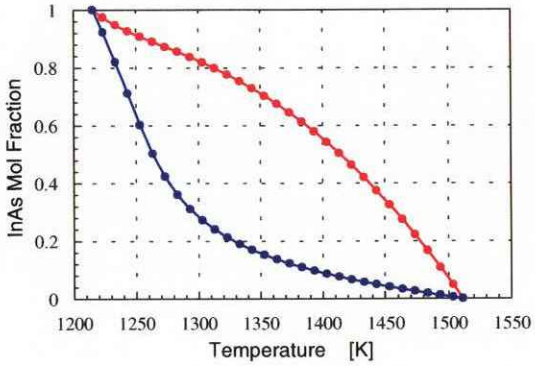

Fig. A-1 Phase Diagram of InGaAs

The phase diagram is determined under the equilibrium state. Therefore, the quasi-equilibrium state is assumed in the model. If the model of the supercooling at the interface is established in future, more precise solutions will be obtained. But the current model should be reliable enough because the growth rate is dominated not by the interfacial reaction rate but by the solute supply rate due to no experimental observation of facets. In such case, both the effect of the anisotropy of the interfacial kinetics on the growth rate and the supercooling at the interface should be small.

In order to solve Eqs. (A-1) – (A-8) numerically, the boundary fitted coordinate (BFC) method, which is a kind of a finite difference method, is used in this study. The BFC method solves the governing equations that are transformed from the physical space to the computational space. Therefore, curved boundaries in the physical space are transformed to linear boundaries. In addition, the coordinates are transformed to the rectangular coordinates in the computational space.

The BFC method has a feature of automatic

grid generation. In this study, the method of the grid generation based on the Poisson equation is used, that is,

$$\xi_{rr}+\xi_{zz}=0, \text{ and} \tag{A-9}$$

$$\eta_{rr}+\eta_{zz}=0, \tag{A-10}$$

where ξ and η are the computational coordinates corresponding to r and z in the physical space, and the subscripts represent the partial differentials. This method is well known as one of the methods of generating a smooth grid. Since Eqs. (A-9) and (A-10) are inconvenient for obtaining the r-z coordinates in the physical space, inverse expressions should be introduced. In order to invert these equations, the relationship between infinitesimal elements in both spaces is required and can be represented as

$$\begin{pmatrix} d\xi \\ d\eta \end{pmatrix}=\begin{pmatrix} \xi_r & \xi_z \\ \eta_r & \eta_z \end{pmatrix}\begin{pmatrix} dr \\ dz \end{pmatrix}, \text{ and} \tag{A-11}$$

$$\begin{pmatrix} dr \\ dz \end{pmatrix}=\begin{pmatrix} r_\xi & r_\eta \\ z_\xi & z_\eta \end{pmatrix}\begin{pmatrix} d\xi \\ d\eta \end{pmatrix}. \tag{A-12}$$

Equation (A-11) can be rewritten as

$$\begin{pmatrix} d\xi \\ d\eta \end{pmatrix}=\frac{1}{J}\begin{pmatrix} z_\eta & -r_\eta \\ -z_\xi & r_\xi \end{pmatrix}\begin{pmatrix} dr \\ dz \end{pmatrix}, \tag{A-13}$$

where J is Jacobian, $r_\xi z_\eta - r_\eta z_\xi$. By comparing Eq. (A-11) with Eq. (A-13), the relationship is obtained as follows;

$$\xi_r=\frac{z_\eta}{J},\ \xi_z=-\frac{r_\eta}{J},$$

$$\eta_r=-\frac{z_\xi}{J},\ \eta_z=\frac{r_\xi}{J}. \tag{A-14}$$

Basing on Eq. (A-14), ξ_{rr}, ξ_{zz}, η_{rr} and η_{zz} can be obtained. For example, ξ_{rr} can be represented as

$$\begin{aligned}\xi_{rr}&=\frac{\partial}{\partial r}\left(\frac{z_\eta}{J}\right)\\&=\left(\xi_r\frac{\partial}{\partial\xi}+\eta_r\frac{\partial}{\partial\eta}\right)\left(\frac{z_\eta}{J}\right)\\&=\xi_r\frac{\frac{\partial z_\eta}{\partial\xi}J-\frac{\partial J}{\partial\xi}z_\eta}{J^2}\\&\quad+\eta_r\frac{\frac{\partial z_\eta}{\partial\eta}J-\frac{\partial J}{\partial\eta}z_\eta}{J^2}\end{aligned} \tag{A-15}$$

The first term and the second one in the right side of Eq. (A-15) are represented as

$$\frac{\frac{\partial z_\eta}{\partial\xi}J-\frac{\partial J}{\partial\xi}z_\eta}{J^2}=\frac{-z_\eta^{\,2}r_{\xi\xi}+z_\xi z_\eta r_{\xi\eta}-r_\eta z_\xi z_{\xi\eta}+r_\eta z_\eta z_{\xi\xi}}{J^2} \tag{A-16}$$

and

$$\frac{\frac{\partial z_\eta}{\partial\eta}J-\frac{\partial J}{\partial\eta}z_\eta}{J^2}=\frac{z_\xi z_\eta r_{\eta\eta}-z_\eta^{\,2}r_{\xi\eta}+r_\eta z_\eta z_{\xi\eta}-r_\eta z_\xi z_{\eta\eta}}{J^2} \tag{A-17}$$

respectively. Equations (A-16) and (A-17) are substituted to Eq. (A-15) and thus the equation is rewritten as follows;

$$\begin{aligned}\xi_{rr}&=\frac{1}{J^3}\left[-z_\eta\left(z_\eta^{\,2}r_{\xi\xi}-2z_\xi z_\eta r_{\xi\eta}+z_\xi^{\,2}r_{\eta\eta}\right)\right.\\&\left.+r_\eta\left(z_\eta^{\,2}z_{\xi\xi}-2z_\xi z_\eta z_{\xi\eta}+z_\xi^{\,2}z_{\eta\eta}\right)\right]\end{aligned} \tag{A-18}$$

By the same way, ξ_{zz} can be obtained as

$$\begin{aligned}&\xi_{zz}\\&=\frac{1}{J^3}\left[-z_\eta\left(r_\eta{}^2\, r_{\xi\xi}-2r_\xi\, r_\eta\, r_{\xi\eta}+r_\xi{}^2\, r_{\eta\eta}\right).\right.\\&\left.+r_\eta\left(r_\eta{}^2\, z_{\xi\xi}-2r_\xi\, r_\eta\, z_{\xi\eta}+r_\xi{}^2\, z_{\eta\eta}\right)\right]\end{aligned} \tag{A-19}$$

Equations (A-18) and (A-19) are substituted to Eq. (A-9) and then,

$$\begin{aligned}&\xi_{rr}+\xi_{zz}\\&=\frac{1}{J^3}\left[-z_\eta\left(\alpha\, r_{\xi\xi}-2\beta\, r_{\xi\eta}+\gamma\, r_{\eta\eta}\right)\right.\\&\left.+r_\eta\left(\alpha\, z_{\xi\xi}-2\beta\, z_{\xi\eta}+\gamma\, z_{\eta\eta}\right)\right]=0\end{aligned} \tag{A-20}$$

is obtained. Equation (A-10) is rewritten by using the same transformation method as

$$\begin{aligned}&\eta_{rr}+\eta_{zz}\\&=\frac{1}{J^3}\left[z_\xi\left(\alpha\, r_{\xi\xi}-2\beta\, r_{\xi\eta}+\gamma\, r_{\eta\eta}\right),\right.\\&\left.-r_\xi\left(\alpha\, z_{\xi\xi}-2\beta\, z_{\xi\eta}+\gamma\, z_{\eta\eta}\right)\right]=0\end{aligned} \tag{A-21}$$

where

$$\alpha=r_\eta^2+z_\eta^2,\quad \beta=r_\xi\, r_\eta+z_\xi\, z_\eta,\ \text{and}$$

$$\gamma=r_\xi^2+z_\xi^2. \tag{A-22}$$

By solving Eqs. (A-20) and (A-21) simultaneously, the following equations are obtained;

$$\alpha\, r_{\xi\xi}-2\beta\, r_{\xi\eta}+\gamma\, r_{\eta\eta}=0,\ \text{and} \tag{A-23}$$

$$\alpha\, z_{\xi\xi}-2\beta\, z_{\xi\eta}+\gamma\, z_{\eta\eta}=0. \tag{A-24}$$

By solving these equations, the coordinates of the nodes in the physical space can be obtained.

The partial differentials by the component corresponding to the physical coordinates, r and z, can be also expressed by using Eq. (A-14), that is,

$$\frac{\partial}{\partial r}=\frac{z_\eta}{J}\frac{\partial}{\partial\xi}-\frac{z_\xi}{J}\frac{\partial}{\partial\eta}, \tag{A-25}$$

$$\frac{\partial}{\partial z}=-\frac{r_\eta}{J}\frac{\partial}{\partial\xi}+\frac{r_\xi}{J}\frac{\partial}{\partial\eta}, \tag{A-26}$$

$$\begin{aligned}&\frac{\partial^2}{\partial r^2}\\&=\frac{1}{J^2}\left(z_\eta{}^2\frac{\partial^2}{\partial\xi^2}\right.\\&\left.-2z_\xi\, z_\eta\frac{\partial^2}{\partial\xi\,\partial\eta}+z_\xi{}^2\frac{\partial^2}{\partial\eta^2}\right)\\&+\xi_{rr}\frac{\partial}{\partial\xi}+\eta_{rr}\frac{\partial}{\partial\eta}\end{aligned} \tag{A-27}$$

$$\begin{aligned}&\frac{\partial^2}{\partial z^2}\\&=\frac{1}{J^2}\left(r_\eta{}^2\frac{\partial^2}{\partial\xi^2}-2r_\xi\, r_\eta\frac{\partial^2}{\partial\xi\,\partial\eta}\right.\\&\left.+r_\xi{}^2\frac{\partial^2}{\partial\eta^2}\right)\\&+\xi_{zz}\frac{\partial}{\partial\xi}+\eta_{zz}\frac{\partial}{\partial\eta}\end{aligned} \tag{A-28}$$

By using Eqs. (A-25) – (A-28), all the governing equations in the physical space can be transformed to the equations in the computational space. Before the physical coordinates are transformed to the computational coordinates, Eqs. (A-5) and (A-6) must be transformed to the scalar expression. In this transformation, it is assumed that the interface shape and its location can be expressed by using any function f, that is,

$$z=f(r,t). \tag{A-29}$$

By using Eq. (A-29), the normal unit vector $\hat{\boldsymbol{n}}$ can be described as

$$\hat{\boldsymbol{n}} = \frac{1}{\sqrt{1+\left(\frac{\partial f}{\partial r}\right)^2}}\left(-\frac{\partial f}{\partial r}, 1\right). \qquad \text{(A-30)}$$

This equation is substituted to the right side of Eq. (A-5);

$$\begin{aligned}&\text{(Right Side)}\\ &\equiv -\kappa_L (\nabla T)_L \cdot \hat{\boldsymbol{n}} + \kappa_S (\nabla T)_S \cdot \hat{\boldsymbol{n}}\\ &= \frac{1}{\sqrt{1+\left(\frac{\partial f}{\partial r}\right)^2}} \qquad \text{(A-31)}\\ &\times\left\{-\kappa_L\left(\frac{\partial T}{\partial z}-\frac{\partial T}{\partial r}\frac{\partial f}{\partial r}\right)\right.\\ &\left.+\kappa_S\left(\frac{\partial T}{\partial z}-\frac{\partial T}{\partial r}\frac{\partial f}{\partial r}\right)\right\}\end{aligned}$$

On the other hand, the left side of Eq. (A-5) is represented as;

$$\text{(Left Side)} = \frac{L_{SL}\,\rho}{\sqrt{1+\left(\frac{\partial f}{\partial r}\right)^2}}\frac{\partial f}{\partial t}. \qquad \text{(A-32)}$$

By combining Eqs. (A-31) and (A-32), Eq. (A-5) can be expressed as

$$\begin{aligned}&L_{SL}\,\rho\frac{\partial f}{\partial t}\\ &=\left\{-\kappa_L\left(\frac{\partial T}{\partial z}-\frac{\partial T}{\partial r}\frac{\partial f}{\partial r}\right)_L\right. \qquad \text{(A-33)}\\ &\left.+\kappa_S\left(\frac{\partial T}{\partial z}-\frac{\partial T}{\partial r}\frac{\partial f}{\partial r}\right)_S\right\}\end{aligned}$$

By using the same transformation, Eq. (A-6) can be also expressed as

$$\begin{aligned}&(C_L - C_S)\frac{\partial f}{\partial t}\\ &= -D_L\left(\frac{\partial C}{\partial z}-\frac{\partial C}{\partial r}\frac{\partial f}{\partial r}\right)_L.\end{aligned} \qquad \text{(A-34)}$$

The governing equations, Eqs. (A-1) – (A-4), (A-33) and (A-34) are transformed from the physical coordinates, r and z, to the computational coordinates, ξ and η. In the transformation, the time differential of the following expression is used;

$$\begin{aligned}&\frac{\partial}{\partial t}\\ &=\frac{\partial}{\partial t'}-\frac{1}{J}\left(z_\eta\frac{\partial}{\partial \xi}-z_\xi\frac{\partial}{\partial \eta}\right)\frac{\partial r}{\partial t'}. \qquad \text{(A-35)}\\ &-\frac{1}{J}\left(-r_\eta\frac{\partial}{\partial \xi}+r_\xi\frac{\partial}{\partial \eta}\right)\frac{\partial z}{\partial t'}\end{aligned}$$

Since t' is actually equal value to t, t' is replaced with t after here.

By substituting Eqs. (A-25) – (A-28) and (A-35) to the governing equations, the transformed expression can be obtained. The energy transport equation, the mass transport equation, the vorticity transport equation, the stream function equation, the energy balance equation and the mass balance equation are described as follows, respectively;

$$\begin{aligned}&\rho\, C_p\left\{\frac{\partial T}{\partial t}-\frac{1}{J}\left(z_\eta T_\xi - z_\xi T_\eta\right)\frac{\partial r}{\partial t}\right.\\ &\left.-\frac{1}{J}\left(-r_\eta T_\xi + r_\xi T_\eta\right)\frac{\partial z}{\partial t}\right\}\\ &-\rho\, C_p\frac{1}{r}\frac{1}{J}\left(\psi_\xi T_\eta - \psi_\eta T_\xi\right) \qquad \text{(A-36)}\\ &=\kappa\frac{1}{J^2}\left(\alpha T_{\xi\xi} - 2\beta T_{\xi\eta} + \gamma T_{\eta\eta}\right)\\ &\qquad +\kappa\frac{1}{r}\frac{1}{J}\left(z_\eta T_\xi - z_\xi T_\eta\right)\end{aligned}$$

$$\frac{\partial C_L}{\partial t}-\frac{1}{J}\left(z_\eta C_{L\xi}-z_\xi C_{L\eta}\right)\frac{\partial r}{\partial t}$$
$$-\frac{1}{J}\left(-r_\eta C_{L\xi}+r_\xi C_{L\eta}\right)\frac{\partial z}{\partial t}$$
$$-\frac{1}{r}\frac{1}{J}\left(\psi_\xi C_{L\eta}-\psi_\eta C_{L\xi}\right) \quad , \quad \text{(A-37)}$$
$$=D_L\frac{1}{J^2}\left(\alpha C_{L\xi\xi}-2\beta C_{L\xi\eta}\right.$$
$$\left.+\gamma C_{L\eta\eta}\right)$$
$$+D_L\frac{1}{r}\frac{1}{J}\left(z_\eta C_{L\xi}-z_\xi C_{L\eta}\right)$$

$$\frac{\partial C_S}{\partial t}-\frac{1}{J}\left(z_\eta C_{S\xi}-z_\xi C_{S\eta}\right)\frac{\partial r}{\partial t}$$
$$-\frac{1}{J}\left(-r_\eta C_{S\xi}+r_\xi C_{S\eta}\right)\frac{\partial z}{\partial t}$$
$$=D_S\frac{1}{J^2}\left(\alpha C_{S\xi\xi}-2\beta C_{S\xi\eta}\right. \quad , \quad \text{(A-38)}$$
$$\left.+\gamma C_{S\eta\eta}\right)$$
$$+D_S\frac{1}{r}\frac{1}{J}\left(z_\eta C_{S\xi}-z_\xi C_{S\eta}\right)$$

$$\frac{\partial \omega}{\partial t}-\frac{1}{J}\left(z_\eta \omega_\xi-z_\xi \omega_\eta\right)\frac{\partial r}{\partial t}$$
$$-\frac{1}{J}\left(r_\eta \omega_\xi-r_\xi \omega_\eta\right)\frac{\partial z}{\partial t}$$
$$+\frac{1}{r}\frac{1}{J^2}\left(-r_\eta \psi_\xi+r_\xi \psi_\eta\right)$$
$$\times\left(z_\eta \omega_\xi-z_\xi \omega_\eta\right)$$
$$-\frac{1}{r}\frac{1}{J^2}\left(z_\eta \psi_\xi-z_\xi \psi_\eta\right)$$
$$\times\left(-r_\eta \omega_\xi+r_\xi \omega_\eta\right)$$
$$-\frac{1}{r^2}\frac{1}{J}\omega\left(-r_\eta \psi_\xi+r_\xi \psi_\eta\right)$$
$$=\nu\frac{1}{J^2}\left(\alpha \omega_{\xi\xi}-2\beta \omega_{\xi\eta}+\gamma \omega_{\eta\eta}\right)$$
$$+\nu\frac{1}{r}\frac{1}{J}\left(z_\eta \omega_\xi-z_\xi \omega_\eta\right)$$
$$-\nu\frac{1}{r^2}\omega+\frac{1}{J}B g\left(z_\eta T_\xi-z_\xi T_\eta\right)$$
$$+\frac{1}{J}G g\left(z_\eta C_\xi-z_\xi C_\eta\right) \quad , \quad \text{(A-39)}$$

$$-r J^2\omega$$
$$=\alpha \psi_{\xi\xi}-2\beta \psi_{\xi\eta}+\gamma \psi_{\eta\eta} \quad , \quad \text{(A-40)}$$
$$-\frac{J}{r}\left(z_\eta \psi_\xi-z_\xi \psi_\eta\right)$$

$$L_{SL}\rho\frac{\partial f}{\partial t}$$
$$=-\kappa_L\frac{1}{r_\xi}\frac{1}{J_L}\left(-\beta T_\xi+\gamma T_\eta\right)_L \quad , \quad \text{(A-41)}$$
$$+\kappa_S\frac{1}{r_\xi}\frac{1}{J_S}\left(-\beta T_\xi+\gamma T_\eta\right)_S$$

$$\left(C_L-C_S\right)\frac{\partial f}{\partial t}$$
$$=-D_L\frac{1}{r_\xi}\frac{1}{J_L}\left(-\beta C_{L\xi}+\gamma C_{L\eta}\right)_L \quad , \quad \text{(A-42)}$$

where subscripts of L and S represent liquid phase and solid phase, respectively. The method of obtaining solutions is summarized and shown in Fig. A-2.

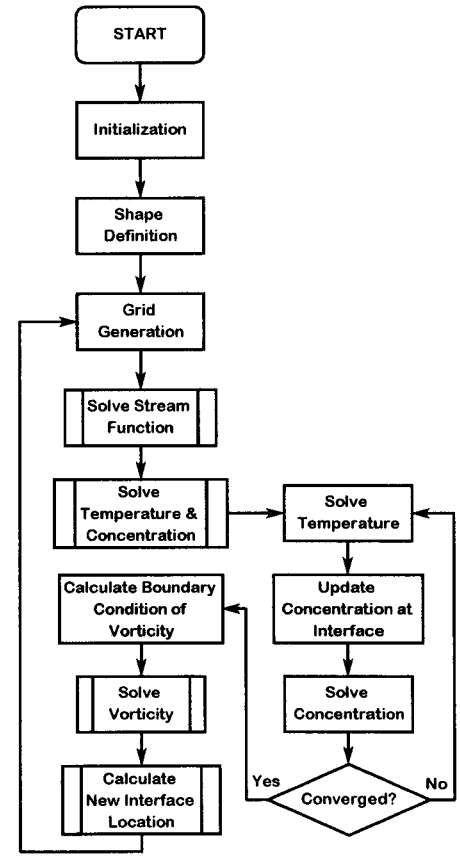

Fig. A-2 Flow Chart

References

1) K. Kinoshita, H. Kato, M. Iwai, T. Tsuru, Y. Muramatsu, S. Yoda: J. Cryst. Growth **225** (2001) 59-66.

2) K. Kinoshita, H. Nakamura, Y. Hanaue, T. Maekawa, M. Tatsumi, M. Yamada, M. Iwai, T. Tsuru, Y. Muramatsu, T. Kuroda, T. Kuwata, H. Hotta: *Growth of* homogeneous $In_{0.3}Ga_{0.7}As$ *single crystals in microgravity*, the proposal to the IAO, http://jem.tksc.nasda.go.jp/utiliz/surp/ar/Semiconductor/PDF%20files/2000/proposal.pdf.

3) J. F. Thompson, F. C. Thames and C. W. Mastin: J. Comp. Phys. **15** (1974) 299.

4) K. Fujii: Numerical *Methods for Computational Fluid* Dynamics (Tokyo Univ., Tokyo, 1994) 2nd ed., Chap. 7 [in Japanese].

5) H. Takami and T. Kawamura: *Numerical Solution of Partial Differential Equations by the Finite Difference Method* (Tokyo Univ., Tokyo, 1994) 2nd ed., Chap. 6 [in Japanese].

6) M. Saitou: Inst. Electron. Mater. Tech. Note **7** (1989) No. 2, 15 [in Japanese].

7) J. S. Szmyd and K. Suzuki (Ed.): *Modeling of Transport Phenomena in Crystal Growth* (WIT Press, Southampton, 2000), Chap. 4.

8) S. Adachi, K. Kawachi, M. Kaneko, H. Kato, S. Yoda and K. Kinoshita: *Reliability Investigation on Numerical Analysis by Comparison with Experimental Result* (Annual Report of the Semiconductor Team in NASDA Space Utilization Research Program, 2000).

9) S. Adachi, S. Yoda, and K. Kinoshita: *Numerical Analysis of a Cartridge in the Traveling Liquidus-Zone Method under Various Gravity Conditions* (Annual Report of the Semicon-ductor Team in NASDA Space Utilization Research Program, 2001).

10) H. Nakamura, Y. Hanaue, H. Kato, K. Kinoshita and S. Yoda: *Quantitative Modeling of the Traveling Liquidus-Zone Growth and Analysis of* $In_xGa_{1-x}As$ *Growth* (To be published).

11) K. Nakajima, T. Kusunoki and C. Takenaka: J. Cryst. Growth **113** (1991) 485-490.